Dynamic measurement of impurity ion transport in runaway electron plateaus in DIII-D

E.M. Hollmann[1,a)], A. Bortolon[2], F. Effenberg[2], N. Eidietis[4], D. Shiraki[3], I. Bykov[4], B.E. Chapman[5], J. Chen[6], S. Haskey[2], J. Herfindal[3], A. Lvovskiy[4], C. Marini[1], A. McLean[7], T. O'Gorman[2], M.D. Pandya[5], C. Paz-Soldan[8], and Ž. Popović[1]

[1] University of California – San Diego, 9500 Gilman Drive, La Jolla, CA 92093-0417 USA
[2] Princeton Plasma Physics Laboratory, PO Box 451, Princeton, NJ 08543-0451 USA
[3] Oak Ridge National Laboratory, PO Box 2008, Oak Ridge, TN 37831, USA
[4] General Atomics, PO Box 85608, San Diego, CA 92186-5608, USA
[5] University of Wisconsin – Madison, 702 W. Johnson St, Madison, WI 53715 USA
[6] University of California – Los Angeles, PO Box 951405, Los Angeles, CA 90095-1405
[7] Lawrence Livermore National Laboratory, 7000 East Avenue, Livermore, CA 94550 USA
[8] Columbia University, 1190 Amsterdam Ave, New York, NY 10027 USA

a) Corresponding author, ehollmann@ucsd.edu

Abstract
The first dynamic (time-dependent) measurements of impurity ion radial (cross-field) and parallel (along-field) diffusion coefficients for post-disruption runaway electron plateaus are presented. Small (~ 1 mm diameter) carbon or silicon pellets are fired into the edge of steady-state runaway electron (RE) plateaus, and the resulting radial and toroidal transport of singly-charged impurity ions (C^+or Si^+) is monitored with spatially distributed visible spectrometers. Consistent with previous steady-state particle balance estimates of Ar^+ radial transport, radial (cross-field) diffusion coefficients $D_\perp \approx 2-5\ \mathrm{m}^2/\mathrm{s}$ are obtained, about 10× larger than expected from neo-classical theory. Parallel diffusion coefficients $D_\parallel \approx 30-80\ \mathrm{m}^2/\mathrm{s}$ are estimated, also much (≈50×) larger than classical. It is speculated at present that these large diffusion coefficients may be due to turbulent transport. Indications of fairly significant (almost 2×) toroidal variation in electron density is seen in the RE plateaus, and this appears to cause some toroidal variation in impurity radial diffusion rates. Indications of slow (≈1 Hz) toroidal rotation in the impurity ions are observed, although the uncertainty in this measurement is large.

I. Introduction

The possibility of first wall damage as a result of disruptions is a significant concern for ITER and other future large tokamak concepts, requiring the development of techniques to minimize wall damage in the event of an unavoidable disruption[1,2,3]. Presently, ITER envisions using a two-step approach for disruption mitigation: first, a mixture of H_2 and Ne will be injected into the disrupting plasma prior to the thermal quench (TQ) to attempt to improve TQ radiation symmetry and minimize localized radiated or conducted heat loads to the first wall. Second, in the event of the subsequent post-current quench (post-CQ) formation of a large current-carrying runaway electron (RE) beam (RE plateau), a further "second injection" of H_2 and Ne could be performed to try to minimize RE-wall strike damage. The material delivery for both first and second injections is planned to be done using shattered pellet injection (SPI)[4,5].

For first injection, it is envisioned to use mostly H_2 and a trace (of order 1%) quantity of neon to give sufficient radiative efficiency for radiating away the initial plasma thermal energy. For the second injection, two distinct approaches have been proposed: low-Z secondary injection, where only H_2 (or D_2) is injected, or high-Z secondary injection, where dominantly Ne (or Ar) is injected. The two approaches have quite different results on the subsequent RE plateau behavior. Low-Z second injection tends to slow RE plateau current dissipation and vertical drift and results in one or two large final loss instabilities when the RE plateau strikes the wall[6,7]. In contrast, high-Z second injection tends to result in increased current dissipation and vertical drift and tends to result in a large number of small final loss instabilities[6,8]. Ion/neutral transport also appears to be quite different in the two approaches. In general, injected pellets appear to be vaporized at the RE plateau edge by RE heating, so ballistic pellet penetration into the plasma appears to be minimal [9,10]. However, for sufficiently large low-Z second injection, the background thermal plasma is cooled by the injected H_2 (or D_2 gas) to the point of volume recombination so that subsequent ion/neutral transport is dominated by neutral diffusion/convection[6]. For high-Z injection, in contrast, neutrals mostly remain excluded from the RE plateau and impurity inventory is dominated by low charge-state ions[11,12].

Choosing between low-Z and high-Z approaches for the ITER 2nd injection is challenging, and complete modeling of the 2nd injection process (including injection, impurity assimilation, vertical drift, final loss instabilities, and RE-wall interaction and melting) has not been undertaken yet, although modeling efforts addressing isolated elements of this process are progressing rapidly[13,14,15]. An important unknown element in this ongoing modeling/prediction effort is the rate of injected impurity ion transport into the RE beam. Impurity ion transport is important for determining the initial RE plateau impurity content and current dissipation; it becomes less important after recombination following low-Z second injection, and then may become important again during the final loss process, if there is re-ionization following final loss instabilities. For high-Z second injection, impurity ion transport is of central importance throughout the RE plateau lifetime.

At present, the only estimates of impurity diffusion into RE beams have been done in a static sense: semi-steady profiles of radiated power and electron density were taken, and the approximate radial diffusion coefficient of the main ion species (Ar^+) needed to balance the ionization source term was estimated. Anomalously large (compared with standard "neo-classical" collisional diffusion) radial diffusion coefficients of order $D_\perp \approx 1 - 5\ \mathrm{m}^2/\mathrm{s}$ were obtained[11].

Here, we present the first measurements of the impurity ion diffusion in a RE plateau using dynamic (time dependent) measurements. Small, non-recycling (carbon or silicon) pellets are fired into the edge of relatively steady-state RE plateaus using an impurity granule injector[16]. The subsequent transport is monitored with visible spectroscopy and analyzed by fitting to a diffusion model; this basic technique has been used quite frequently for impurity transport studies in thermal plasmas in tokamaks[17], stellarators[18], and linear devices[19]. Consistent with the previous steady-state particle balance estimates, radial (cross-field) diffusion coefficients $D_\perp \approx 2 - 5\ \mathrm{m}^2/\mathrm{s}$ are obtained. A slight increase in $D_\perp$ with decreasing mass is indicated by the data. The data suggests that $D_\perp$ increases with plasma density and is toroidally asymmetric, i.e. radial diffusion appears faster on the side of the machine with larger electron density. Estimates of

toroidal transport are also obtained. Parallel diffusion coefficients $D_{\parallel} \approx 30 - 80\ \mathrm{m}^2/\mathrm{s}$ are obtained, also much (≈50×) larger than classical. Some indications of slow (≈1 Hz) toroidal rotation in the impurity ions are observed, although the uncertainty in this measurement is of order unity. Overall, the results of this paper indicate that impurity ion diffusion timescales (radial and toroidal) will be significantly slower than vertical drift timescales in future reactor-scale tokamaks. Predicting the effectiveness of impurity injection at mitigating RE-wall damage in these future devices will therefore need to take into account the possibility of incomplete mixing at the time of RE-wall impact.

II. Experimental setup

The experiments described here were performed on the DIII-D tokamak[20]. An overview of the main diagnostics and pellet injectors used here is shown in Fig. 1. Two pellet launchers are used for the impurity transport experiments, both firing into the plasma outer midplane – a cryogenic argon pellet injector at toroidal angle $\phi = 135°$ and a solid (C or Si) pellet injector at toroidal angle $\phi = 270°$. Separately, a third pellet injector is used only for imaging the solid (C) pellet + RE beam interaction; this pellet injector has a vertical upward launch at $\phi = 150°$. The main diagnostic used here to measure impurity transport is a 12-chord tangentially-viewing visible spectrometer array, shown by red view chords in Fig. 1(a). Additional important diagnostics include Thomson scattering to measure plasma electron temperature and density, two interferometers to measure electron line density at two different toroidal angles[21,22], a foil bolometer array to measure total radiated power, and a downward-viewing UV spectrometer.

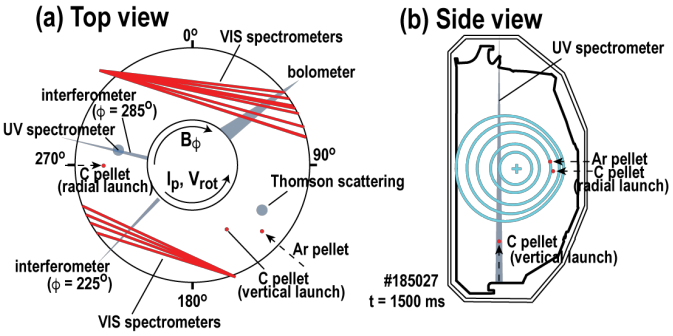

Fig. 1. (a) Top and (b) Side views of DIII-D tokamak showing main diagnostics and pellet injectors used in these experiments

Time traces outlining the time sequence of these experiments is shown in Fig. 2. First, an inner wall-limited deuterium plasma is ramped to 1.2 MA toroidal current and shut down at time t = 1200 ms with cryogenic Ar pellet injection, Fig. 2(a). Gyrotron heating, Fig. 2(b), is used to produce a fairly hot (2 – 3 keV) initial target plasma which will give significant RE production during shut down. In the shot shown in Fig. 2, the central pre-disruption (t = 1190 ms) electron

density is $n_e = 2.5 \times 10^{13}$ cm^{-3}, while the central pre-disruption electron temperature is $T_e =$ 2.8 keV. Strong RE formation can be seen from the large hard x-ray (HXR) signal from the RE plateau which forms at t = 1200 ms. This plateau is held fairly constant in current and position until t = 1600 ms, at which point the current channel is pushed downward and allowed to terminate on the lower divertor.

In the middle of the RE plateau, typically around t = 1400 – 1500 ms, a small solid pellet (C or Si) is fired into the RE plateau radially, giving a small pulse of impurities at the RE plateau edge. The Ar pellets used contain 15 Torr-L of Ar, while the initial electron density and deuterium number of the target plasma is approximately 5 Torr-L, so the resulting RE plateau is expected to consist of roughly 15 Torr-L Ar and 5 Torr-L D. The small solid (C or Si) impurity pellet contains approximately 1 Torr-L of atoms, which is expected to cause relatively little perturbation to the global RE plateau dynamics. Consistent with this, a small (~10%) perturbation to local electron density is seen on carbon pellet impact, Fig. 2(d), but no significant changes to loop voltage, global radiated power, or electron temperature are seen, Fig. 2(e-g).

The centered RE plateaus used in these experiments are usually quite MHD stable. For example, in the middle of the RE plateau in Fig. 2, t = 1500 ms, toroidal magnetic field is B_T= 2.1 T, toroidal current is I_P = 240 kA, and edge safety factor is quite high, $q_a \approx 6$.

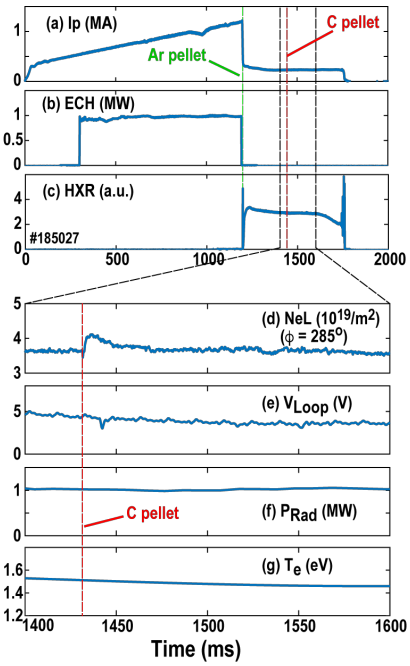

Fig. 2. Experimental time traces showing (a) plasma current, (b) gyrotron power, and (c) hard x-ray signal; and zoomed time traces showing (d) line electron density, (e) loop voltage, (f) radiated power, and (g) central thermal plasma electron temperature (from Thomson scattering).

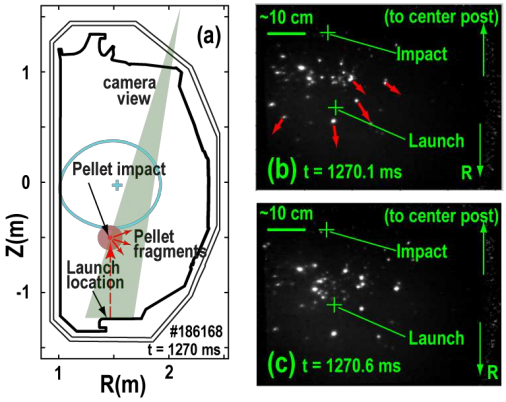

Fig. 3. Imaging of C pellet injection into RE plateau from below, showing (a) camera view geometry and (b,c) images of exploding C pellet fragments at two time steps. Red arrows show velocity vectors for several fragments.

The deposition of C (or Si) from the second impurity pellet is expected to be highly localized in time (~ 1 – 2 ms) and space (~40 cm toroidally) relative to experimental time scales (50 ms) and dimensions (5 m toroidally), as discussed below. REs are expected to cause rapid volumetric heating throughout the injected pellet volume, leading to explosion of the pellet at the RE beam edge[9,23]. Although imaging of the pellet/plasma interaction region was not visible for the $\phi = 270°$ injection, visible camera imaging for similar (solid 1 mm carbon) pellets was available for pellets launched upward from below the RE plateau, as shown in Fig. 3. This imaging did see the pellet exploding into glowing fragments with apparent fragment velocities of order 50 m/s, and a small apparent impurity deposition region perhaps 40 cm across (poloidal/toroidal extent). This is supported by previous imaging of plastic pellet injection into RE plateaus[9] and also experiments with neon shattered pellet injection into RE plateaus, which found deposition characteristics very similar to gas injection to the RE plateau edge[10]. These images cannot accurately separate radial and poloidal positions of the fragments, so the radial deposition profile resulting from the impurity pellet is not known, but is thought to be fairly shallow (perhaps 10 cm), i.e. mostly confined to the RE plateau edge.

III. Data analysis

The principal diagnostic used here to study impurity ion transport in the RE plateau is a multi-chord visible spectrometer, Fig. 1(a). Data is taken along 12 tangential view chords, but typically a subset (perhaps half) of these are used in the analysis, since additional view chords are not found to significantly improve constraint of the diffusion coefficients past a certain point.

Sample spectra are shown in Fig. 4. The main lines used in these experiments are C-II 658 nm (to study C^+ transport) and Si-II 598 nm (to study Si^+ transport). C-II lines can be seen to clearly increase following C pellet injection, while Si-II lines are shown to clearly increase following Si pellet injection.

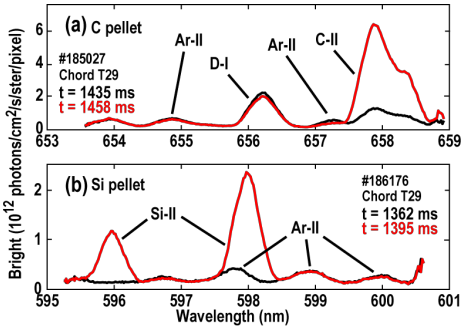

Fig. 4. Sample visible spectrometer spectra before (black curves) and after (red curves) impurity pellet injection showing (a) C-II lines following C pellet injection and (b) Si-II lines following Si pellet injection.

As can be seen in Fig. 4, the visible spectra can be complicated by the presence of initial "intrinsic" carbon C-II lines and the presence of Ar-II lines. These line contributions are corrected for with the use of "reference" shots, with the same experimental conditions but no impurity pellet injection, as illustrated in Fig. 5. Figure 5(a) shows time traces of line brightnesses showing C-II and Ar-II as a function of time following C pellet injection. Figure 5(b) shows the same measurements but for a reference shot. To arrive at the "pulsed" C-II signal (due to carbon from the pellet only), it is assumed that any Ar-II contribution in the C-II bandpass has the same time dependence as the nearly Ar-II line (654.8 nm). Additionally, it is assumed that the intrinsic C-II signal during the pellet shot has the same time dependence as the C-II signal during the reference shot. The Ar-II and intrinsic C-II contributions are then estimated by scaling the reference shot C-II and Ar-II signals linearly to best match the pre-pellet C pellet shot data. This scaling factor is normally quite close to unity (0.9 to 1.1), as the shots are fairly repeatable. After this background subtraction, the pulsed C-II brightness, Fig. 5(c) is obtained. Similar analysis is done for Si pellet injection shots to correct for Ar-II, although in this case there is no intrinsic impurity signal, so only the Ar-II line at 597.8 nm needs to be subtracted.

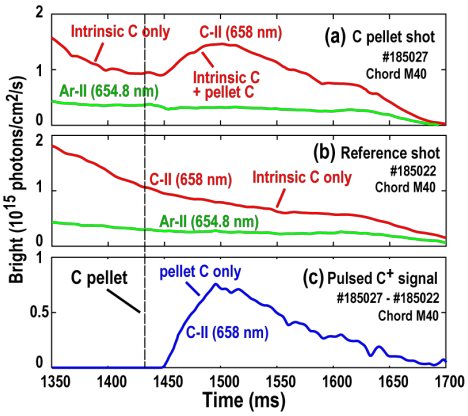

Fig. 5. Time traces of (a) C-II and Ar-II brightness for a shot with C pellet injection, (b) C-II and Ar-II brightness in a shot without C pellet injection, and (c) the background-subtracted pulsed C-II brightness.

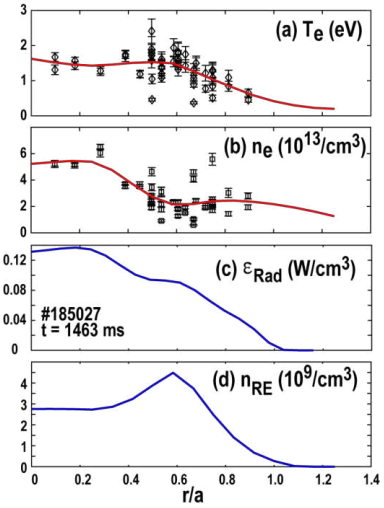

Fig. 6. Radial profiles of (a) thermal electron temperature from TS, (b) thermal electron density from TS, (c) radiated emissivity from the bolometer array, and (d) runaway electron density estimated from the radiated emissivity profile.

To interpret the measured impurity line brightnesses, it is necessary to know the background plasma electron density and temperature. The impurity line brightness will be proportional to impurity ion density and roughly proportional to electron density (some deviation from linearity with n_e occurs at due to the presence of REs and due to collisional-radiative effects). We

approximate the RE plateau plasma as consisting of a thermal background plasma with temperature T_e, and density n_e, plus a mono-energetic RE plasma with effective density n_{RE}. T_e and n_{RE} are assumed to be functions of minor radius $\rho = r/a$ only. A constant RE kinetic energy $K_{RE} = 10$ keV is assumed at all radii, as justified later. In the data analysis, we allow for an $n = 1$ (cos) toroidal variation in n_e. As mentioned above, the RE plateau contains about 15 Torr-L of Ar, 5 Torr-L of D, and (after C pellet injection) 1 Torr-L of C, so Ar^+ is the dominant ion species in the RE plateau and will dominantly determine the electron density. During the TQ/CQ of rapid shutdowns caused by Ar injection, Ar ion toroidal transport is reasonably rapid, with a 2 – 3 ms toroidal transport timescale in DIII-D [24]. However, shutdown by Ar pellet injection is quite rapid (TQ + CQ duration ~ 5 ms) and Ar ions are not necessarily fully toroidally mixed by the RE plateau onset, at which point ion toroidal transport becomes very slow, with a >100 ms timescales. This is demonstrated later in the paper where parallel ion diffusion coefficients of order $D_\parallel \approx 30 - 80\ \mathrm{m^2/s}$ are obtained; together with a toroidal distance scale length (half way around the torus) of order 5 m, this gives a toroidal diffusion time scales of order 300 – 800 ms. n_e is assumed to be a separable function of minor radius and a cosine toroidal shape: $n_e = A(\rho) \times \left(1 + B\cos\left(\phi - \phi_{peak,N}\right)\right)$ with the radial shape determined by the TS profile at $\phi = 120^\circ$, Fig. 6(a). Ar^+ is assumed to have the same toroidal structure $n_{Ar+} \sim \left(1 + B\cos\left(\phi - \phi_{peak,N}\right)\right)$, so that the total radiated emissivity (dominated by Ar ion line emission and roughly proportional to $n_e n_{Ar+}$) can be assumed to have a $\left(1 + B\cos\left(\phi - \phi_{peak,N}\right)\right)^2$ toroidal dependence, corresponding roughly to a $\cos^2$ shape. The coefficients A and B and the toroidal angle of peak density $\phi_{peak,N}$ can be estimated by fitting to line-integrated density measurements at different toroidal locations, as well as line-integrated Ar-II brightness at different toroidal locations, as shown in Fig. 7. Typically, peak density angles in the vicinity $\phi_{peak,N} \approx 60^\circ$ are obtained, indicating that the peak plasma density is slightly counterclockwise from the Ar pellet injection location $\phi = 135^\circ$. The peak density angle typically appears to rotate slightly during the course of the experiment, Fig. 7(c). As expected, the overall amplitude of the electron density toroidal asymmetry slowly decreases over time during the RE plateau lifetime, Fig. 7(d). Two similar shots with different carbon pellet injection times are shown in Fig. 7(c, d) to illustrate that the change in peak density angle and decay in density asymmetry seen in the data are roughly repeatable shot-shot and are only slightly perturbed by the smaller C pellet injection.

The effective RE density profile can be estimated for a given RE kinetic energy K_{RE}, using the known stopping power of fast electrons on impurity ions and atoms, and balancing this with the reconstructed radiated emissivity profile, Fig. 6(c). This neglects radial heat transport by ions or neutrals compared with radiative loss, which is expected to be a reasonable assumption for these plasmas[6]. This also neglects UV line trapping, which is not expected to be entirely negligible in these plasmas, but correcting the reconstructed radial emissivity profile for UV line trapping is extremely challenging and is not attempted here. The choice $K_{RE} = 10$ keV is much lower than the typical (K~ 1 MeV) or upper (K~ 10 MeV) kinetic energies in the RE energy distribution function but is used because it is the upper electron energy presently allowed in the PrismSPECT collisional-radiative code [25]. The precise energy chosen for K_{RE} is not expected to be important here, as long as K_{RE} is chosen much greater than typical excitation energies of importance, since RE density n_{RE} is a scalable parameter. The approximate magnitude of the error introduced by this approximation in the collisional-radiative model kinetics can be estimated by looking at the

ratio of excitation rates to lowest-lying electronic states versus those of highest-lying electronic states. For Ar^+, the lowest lying energy levels lie approximately 13 eV above the ground state, while the highest energy levels lie about 27 eV above the ground state. In the Bethe approximation[26], the electron-impact excitation cross-section of a dipole transition has an electron kinetic energy K dependence $\sigma \sim 1/K$, so there is no error introduced by changing K_{RE}, i.e. $\frac{\sigma_{13}}{\sigma_{12}}(K = 10\text{ keV})/\frac{\sigma_{13}}{\sigma_{12}}(K = 1\text{ MeV}) = 1$, where $\frac{\sigma_{13}}{\sigma_{12}}$ is the dipole excitation rate going from ground state to 27 eV upper states divided by excitation rate going from ground to 13 eV upper states. In the plane Born approximation with BE scaling, the cross section has a kinetic energy dependence $\sigma \sim 1/(K + E + B)$, where E is the excitation energy and B is the binding energy[27]. This results in a ratio $\frac{\sigma_{13}}{\sigma_{12}}(K = 10\text{ keV})/\frac{\sigma_{13}}{\sigma_{12}}(K = 1\text{ MeV}) \approx 0.9986$, i.e. an error of less than 0.2%.

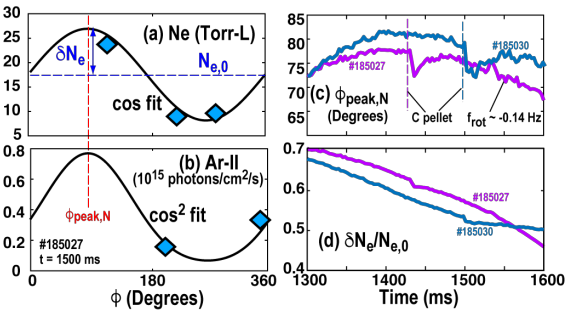

Fig. 7. (a) Line-integrated electron density and (b) line-integrated Ar-II brightness as a function of toroidal angle, as well as cos and $\cos^2$ fits; and (c) toroidal angle of peak density vs time and (d) thermal electron density toroidal asymmetry amplitude vs time.

Once the background density and temperature have been estimated, the expected line-integrated impurity line brightness (C-II or Si-II) can be estimated for a given spatial impurity distribution. Here, we assume that the injected impurities are non-perturbative, so (small) local changes in electron density or temperature due to the presence of the small impurity injection are ignored, although the slow evolution of electron temperature, as captured by the bolometers and TS, and toroidal variation of electron density, fit as discussed above, are included. C-II and Si-II line brightnesses are estimated using PrismSPECT. Thermal and RE excitation is included simultaneously with the REs approximated as mono-energetic as discussed above. The simulations are local to each radius, although the (small) effect of UV line opacity on visible line emission is approximated using a homogenous slab escape factor approximation. The simulations are run non-equilibrium in charge state, since charge state equilibrium can take tens of ms to achieve in these conditions. Injected atoms are initialized as neutrals and tracked through charge states during their diffusion through the plasma. The equilibrium charge state distribution in these plasmas is typically dominantly singly ionized, but with a non-negligible fraction of doubly ionized ions.

The effect of RE excitation on visible lines is found to be non-negligible in these experiments. This is illustrated in Fig. 8, which shows measured and predicted C-II and C-III line brightnesses

from intrinsic carbon as a function of time during a reference shot (without C pellet injection). To predict intrinsic carbon brightness, a uniform carbon fraction is assumed initially (at the start of the RE plateau). This fraction and a single radial diffusion coefficient are then varied in a 1D (radial) diffusion model to best match the line-integrated C-II brightness vs time (including both thermal and RE excitation), shown by the red curves in Fig. 8(a). Turning off RE excitation gives a drop of about 4× (initially) and 10× (at the end of the shot) in predicted C-II brightness, black curve in Fig. 8(a). The effect is even more dramatic for C-III, where a drop of 100× (initially) and 1000× (at the end of the shot) is predicted for C-III brightness. It can be seen in Fig. 8(b) that C-III is poorly matched, even when including RE excitation. UV lines are much more affected by opacity here than visible lines and are therefore much more challenging to model; visible lines are therefore used for this study.

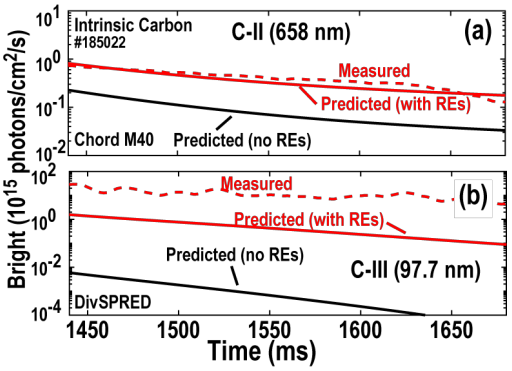

Fig. 8. Measured and modeled intrinsic carbon line brightnesses vs time with and without RE impact excitation included for a shot without C injection showing (a) C-II 658 nm and (b) C-III 97.7 nm.

To match line-integrated visible C-II line brightnesses for C injection experiments (or Si-II line brightnesses for Si injection experiments), a 3D diffusion model is used. Cross-field poloidal diffusion is assumed to be the same as radial diffusion, so the main free parameters varied in the diffusion model are $D_{\perp,min}$, $D_{\perp,max}$, $D_{\parallel}$, f_{rot}, and m_{pel} . These free parameters are assumed constant in time and spatially throughout the diffusion experiment. $D_{\perp,min}$ and $D_{\perp,max}$ are the minimum and maximum perpendicular (radial) diffusion coefficients, with the maximum being at toroidal angle $\phi = \phi_{peak,D}$ and a cosine shape filling in the toroidal variation of $D_{\perp}$ between $D_{\perp,min}$ and $D_{\perp,max}$. There is no physics basis for this cos shape, but this shape could be reasonable if, for example, $D_{\perp}$ is proportional to n_e (which is also being fit to a cos shape toroidally). Typically, it is assumed that $\phi_{peak,D} = \phi_{peak,N}$, i.e. the toroidal peak in diffusion occurs at the same location as the toroidal peak in density. This assumption was tested by a sensitivity scan where $\phi_{peak,D}$ was varied, shown later, confirming that $\phi_{peak,D} \approx \phi_{peak,N}$ within the scatter of the data. m_{pel} is the injected pellet mass. The impurity pellets have a pellet-to-pellet size variation of about a factor of 2 and unknown deposition efficiency after shattering, so the pellet mass is left as a free parameter and varied to best match the data. The pellet impact

time at the plasma is taken from the rise in local electron density, Fig. 2(d), cross-checked with the timing of a local photodiode measurement of pellet light. The initial neutral deposition is assumed to be localized toroidally and poloidally to the pellet injection location with a 50 cm diameter poloidal/toroidal spot size and at minor radius of $\rho = 0.8$. A sensitivity study was performed and showed that the precise deposition depth (e.g. $\rho = 0.7$ vs $\rho = 0.8$) and width (e.g. a 30 cm spot size vs a 50 cm spot size poloidally) did not significantly affect the resulting predicted signals at the toroidally distant visible spectrometers. Poloidal transport due to field line helicity moving toroidally around the tokamak was included in the model but was found to produce only a small (~5%) change in the resulting fit values of $D_\perp$, which is small compared with the uncertainty typically estimated from the fit quality (~25%).

Figure 9 shows line-integrated pulsed C-II brightness data and fits to the data using the 3D diffusion model. It can be seen that reasonably good fits (typically within better than 10%) to the time traces can be achieved. For clarity, four view chords are shown here, although fits can be done to all 12 available view chords, with similar results. It can be seen that the toroidally closer view chords T29 and T31 (around $\phi = 200°$) see signal first but then the radially deeper, toroidally more distant view chords M01 and M40 (around $\phi = 0°$) take longer to decay. The initial signal rise more strongly constrains the toroidal rotation and diffusion in the 3D model, while the signal decay more strongly constrains the radial diffusion.

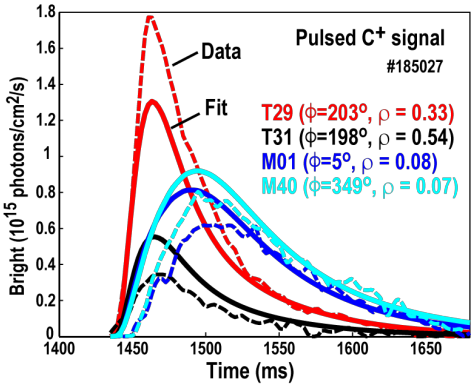

Fig. 9. Time traces of pulsed line-integrated C-II brightnesses for a C pellet injection experiment showing measurements (solid curves) and fits using 3D diffusion model (dashed curves). Values of toroidal angle ϕ and minor radii ρ refer to point of minimum ρ for each view chord.

IV. Results

Radial diffusion coefficients as a function RE plateau current are shown in Fig. 10. The points marked "C^+ data" and "Si^+ data" are from the C and Si pellet injection experiments with 3D diffusion model fits, as discussed above. Toroidally average values $D_\perp = (D_{\perp,min} + D_{\perp,max})/2$ are shown. The main result of this data is that the radial diffusion coefficients are quite large,

typically of order $D_\perp \approx 2-5\ \mathrm{m^2/s}$. These values are roughly consistent with estimates of Ar^+ ion radial diffusion in the RE plateau made from a steady-state 1D diffusion model, described previously, which balances the ionization source term of Ar ions with radial loss to the wall of Ar ions. Some rise in $D_\perp$ with I_P may be indicated in this data, although this is only seen in one data point, so the statistics are poor. The mass dependence of $D_\perp$ does not appear very strong, although there is some indication of a slight decrease in $D_\perp$ with mass when comparing C and Si data points.

The dashed curves in Fig. 10 show estimates of cross-field diffusion coefficients from neo-classical theory. In the RE plateau plasmas, assuming ion temperatures $T_i \approx T_e$, most ions are in a medium-high collisionality regime $\rho_i < \lambda < qR$, where ρ_i is the gyro-radius, λ is the ion mean free path, q is the safety factor and R is the major radius. A small fraction of ions are in the high collisionality regime $\lambda < \rho_i$. The neo-classical radial diffusion coefficient is expected to be of order $D_{\perp,B} \approx \nu\rho_i^2$ in the magnetized fluid regime $\lambda \approx \rho_i$, where ν is the ion-ion collision frequency, and of order $D_{\perp,PS} \approx q^2\nu\rho_i^2$ in the Pfirsch-Schluter regime $\lambda \approx qR$. Here a simple interpolation is done between these two, i.e. it is assumed $D_\perp = D_{\perp,B}$ at $\lambda = \rho_i$ and increases linearly to $D_\perp = D_{\perp,PS}$ at $\lambda = qR$. For highly collisional ions with $\lambda < \rho_i$, the unmagnetized fluid diffusion coefficient $D_{UM} \approx \nu\lambda^2$ is used. The dashed curves in Fig. 10 are profile-averaged neo-classical diffusion coefficients for different species. These can be seen to be of order $D_\perp \approx 0.2-0.5\ \mathrm{m^2/s}$, so about 10× lower than the measured diffusion coefficients. The assumption $T_i \approx T_e$, used here is expected to be realistic, since ion-electron temperature equilibration timescales τ_{ie} are quite short: even for heavy Ar^+ ions, $\tau_{ie} \approx 0.5$ ms, so much shorter than ion transport timescales. Ion temperature has been measured spectroscopically for C^+ ions in these plasmas and T_i = 1.6 eV was measured [28], consistent with $T_i \approx T_e$. If T_i were slightly different from T_e, it would not affect the comparison if Fig. 10 significantly, since neo-classical diffusion is only weakly dependent on T_i , i.e. $D_{\perp,B} \sim T_i^{-1/2}$.

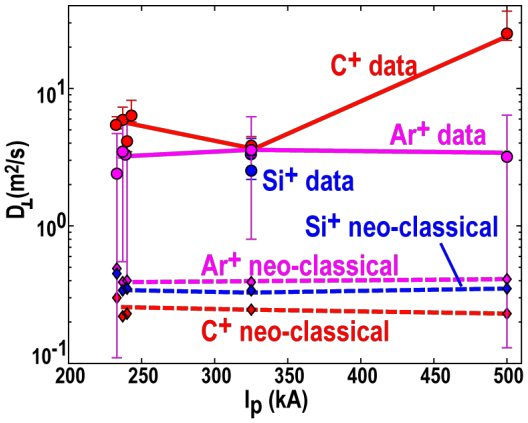

Fig. 10. Measured cross-field diffusion coefficients (circles) vs plasma current, as well as neo-classical values (diamonds).

The measured cross-field diffusion coefficients displayed in Fig. 10 are a toroidal average; as discussed above, the fits actually indicate that $D_\perp$ is higher on the high density side of the machine. This toroidal variation is illustrated in Fig. 11(a), which shows $D_{\perp,min}$ (points at lower n_e) and $D_{\perp,max}$ (points at higher n_e) for C and Si. Overall, despite the large scatter in the data, it can be seen that there appears to be a clear increase toroidally in $D_\perp$ from the low density ($\phi = \phi_{peak,N} - \pi$) to high density ($\phi = \phi_{peak,N}$) side of the machine.

Figure 11(b) shows the toroidal angle of peak density $\phi_{peak,N}$ for different shots, as well as the toroidal angle of peak diffusion $\phi_{peak,D}$ obtained by allowing this to be a free parameter in the diffusion model. It can be seen that the two peaks coincide within the scatter of the data, so peak radial diffusion occurs at peak density toroidally. This peak can be seen to be slightly rotated counterclockwise away from the Ar pellet injection location. Overall, the data indicates that the radial diffusion increases with density and therefore rises to a peak at toroidal angle of peak density $\phi_{peak,N}$. Overall, the method of fitting to peak density $\phi_{peak,N}$ appears to be more strongly constrained and direct than the angle $\phi_{peak,D}$ obtained from the diffusion model. Therefore, the diffusion and rotation coefficients shown here, Fig. 11a, and Fig. 12, do not keep $\phi_{peak,D}$ as a free parameter and instead force $\phi_{peak,D} = \phi_{peak,N}$, thus reducing the number of free parameters in the diffusion model.

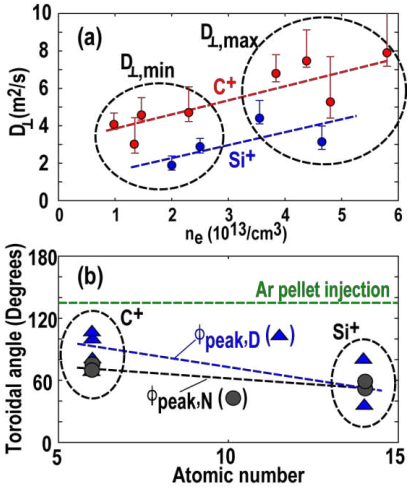

Fig. 11. (a) Variation in radial diffusion coefficient with electron density showing higher diffusion coefficient at higher density at similar plasma current. Dashed lines are simply linear fits to data. (b) Toroidal angle of peak diffusion and toroidal angle of peak density vs impurity ion atomic number at similar plasma current, showing that peak density occurs slightly counterclockwise from Ar pellet injection location and also that peak density and peak diffusion occur roughly at same toroidal location.

Figure 12 shows data on toroidal transport of injected impurities at similar plasma current. Fig. 12(a) shows the fit parallel diffusion coefficient $D_{\|}$, while Fig. 12(b) shows the fit toroidal impurity rotation frequency f_{rot}. Overall, it can be seen that the parallel diffusion is fairly rapid, $D_{\|} \approx 30 - 80\ \mathrm{m}^2/\mathrm{s}$. Expected profile-averaged classical parallel diffusion $D_{\|} \approx D_{UM} \approx \nu\lambda^2$ is shown by red points in Fig. 12(a); these points can be seen to be of order $D_{\|} \approx 2 - 4\ \mathrm{m}^2/\mathrm{s}$, so about 20× lower than the measurements.

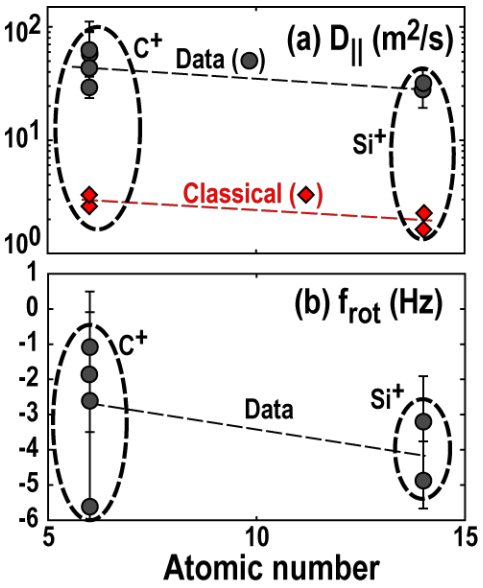

Fig. 12. (a) parallel diffusion coefficient data and collisional theory, and (b) impurity toroidal rotation frequency vs impurity ion atomic number at similar plasma current.

V. Discussion

The main result of this work is an improved measurement of the radial diffusion coefficient in a RE plateau and a first estimate of the parallel ion diffusion coefficient. Previous estimates of the radial diffusion coefficient have been done but involved a steady-state ionization balance and had much larger uncertainty than the pulsed deposition experiments done here. In both radial and parallel directions, the diffusion is found to be much (10× or more) larger than expected for classical collisional diffusion, suggesting a contribution from turbulence, such as for example, drift wave turbulence, which is known to enhance transport in highly collisional, cold plasmas [29]. Another possibility is a strong radial ion mobility. These RE plateaus do appear to have a large positive plasma potential[11], so it is possible that there is an enhanced radial ion loss due to the resulting positive radial electric field.

At present, it is not known what the size scaling of RE plateau anomalous impurity diffusion is. However, assuming no or weak size scaling as a starting point, it is clear that high-Z 2nd injection in ITER will give an extremely inhomogeneous impurity deposition in the RE plateau. The RE plateau vertical drift time scale (and RE plateau lifetime) in ITER is expected to be of order 100 ms [30]. Assuming $D_{\|} = 50\ \mathrm{m}^2/\mathrm{s}$ gives a time scale for impurities to go halfway around ITER toroidally of about 8 s. The time scale to reach the center of the RE plateau in ITER by radial diffusion, assuming edge deposition and $D_{\perp} = 2\ \mathrm{m}^2/\mathrm{s}$ is about 2 s, so also much longer than the RE plateau lifetime. Future modeling to try to predict the effect of 2nd injection in ITER will therefore need to take into account the possibility of this very slow and incomplete impurity mixing during the RE plateau lifetime.

In the analysis above, sputtering from the wall during the experiments was ignored. Comparison between pulsed and intrinsic carbon decay rates indicates that wall sputtering is a small (of order 1%) effect in the pulsed deposition experiments and can therefore be ignored. As an example, Fig. 13 shows pulsed and intrinsic carbon number as a function of time, estimated from fits to C-II brightnesses using 3D and 1D models, respectively. It can be seen that, at early times, there is of order 1 Torr-L of pulsed carbon and of order 0.2 Torr-L of intrinsic carbon in the plasma. The decay time scale of pulsed carbon is of order 100 ms, compared with about 300 ms for intrinsic carbon. Assuming a wetted area of about 10 m^2, the plasma is interacting with (trying to sputter) of order 15 Torr-L (5×10^{20}) C atoms on the wall. Setting the diffusive loss time scale of intrinsic carbon to 100 ms, the 300 ms intrinsic decay time scale gives an estimated sputtering time scale of 10 s for wall carbon atoms. The relative effect of sputtering on the pulsed (background subtracted) carbon signal can then be estimated by comparing 1 Torr-L/0.1 s ≈ 10 Torr-L/s diffusive loss rate with 1 Torr-L/10 s ≈ 0.1 Torr-L/s sputtering rate of pulsed carbon ions, giving a 1% effect.

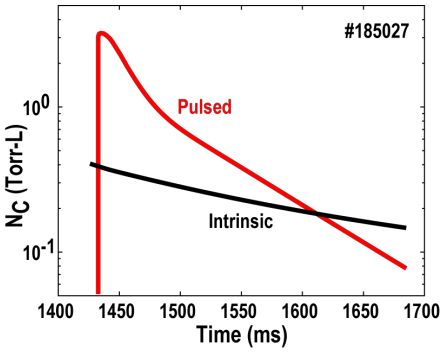

Fig. 13. Pulsed and intrinsic carbon content vs time showing difference in carbon content decay rates.

In addition to the main focus of measuring radial impurity diffusion, this work has shown some evidence for toroidal impurity ion rotation in the RE plateau. The fits to the rotation of the electron density peak seem to give fairly slow counterclockwise toroidal rotation values of order 0.1 – 0.2 Hz in the middle of the RE plateau, Fig. 7(c). On the other hand, the fits to the transient carbon or silicon ion impurity diffusion tend to somewhat larger toroidal rotation values of order

1 – 3 Hz, Fig. 12(b). At present, it is not clear how to reconcile these two different results. It is perhaps plausible that the toroidal electron density asymmetry is maintained by larger local recycling, from e.g. a weak $n = 1$ kink structure leaning on the center post or a higher density neutral Ar cloud remnant from the initial Ar pellet injection. The faster net ion rotation could perhaps be driven by a different mechanism, such as ion orbit loss [31]. Even at several Hz, however, this effect is fairly small (acting on a 1 s timescale) and does not dominate the impurity ion toroidal transport.

In conclusion, impurity ion diffusion (radial and toroidal) in the RE plateau is measured here for the first time using transient (pulsed) impurity deposition into the RE plateau. If applicable to larger tokamaks, these results suggest that radial and toroidal impurity transport will be significantly slower than vertical drift timescales in future reactor-scale tokamaks. It could therefore be that massive high-Z injection for RE plateau current dissipation will be less effective than is observed in present devices. Predicting the effectiveness of impurity injection at mitigating RE-wall damage in future devices will therefore need to take into account the possibility of incomplete impurity mixing.

Acknowledgements

This work was supported in part by the U.S. Department of Energy under DE-FG02-07ER54917, DE-FC02-04ER54698, DE-AC02-09CH11466, DE-AC05-00OR22725, DE-AC52-07NA27344, DE-FG02-04ER54744, and DE-AC05-06OR23100. Technical support of L. Chousal, J. Kulchar, and D. Ayala is gratefully acknowledged, as is diagnostic support of M. Austin, C. Chrystal, C. Lasnier, A. Moser, and M. Van Zeeland. Permission to use PrismSPECT from I. Golovkin is gratefully acknowledged.

References

[1] M. Lehnen, K. Aleynikova, P.B. Aleynikov, D.J. Campbell, P. Drewelow, N.W. Eidietis, Yu. Gasparyan, R.S. Granetz, Y. Gribov, N. Hartmann, E.M. Hollmann, V.A. Izzo, S. Jachmich, S.H. Kim, M. Kocan, H.R. Koslowski, D. Kovalenko, U. Kreuzi, A. Loarte, S. Maruyama, G.F. Matthews, P.B. Parks, G. Pautasso, R.A. Pitts, C. Reux, V. Riccardo, R. Roccella, J.A. Snipes, A.J. Thornton, P.C. de Vries, and EFDA JET contributors, J. Nucl. Mater. 463, 39 (2015).
[2] E.M. Hollmann, P.B. Aleynikov, T. Fülöp, D.A. Humphreys, V.A. Izzo, M. Lehnen, V.E. Lukash, G. Papp, G. Pautasso, F. Saint-Laurent, and J.A. Snipes, Phys. Plasmas 22, 021802 (2015).
[3] B.N. Breizman, P.B. Aleynikov, E.M. Hollmann, and M. Lehnen, Nucl. Fusion 59, 083001 (2019).

[4] T.E. Gebhart, L.R. Baylor, M.N. Ericson, S.J. Meitner, A.L. Qualls, and D.A. Rasmussen, Nucl. Fusion 61, 106007 (2021).
[5] M. Lehnen, "The ITER Disruption Mitigation System – Design progress and design validation," (PPPL Workshop on Theory & Simulations of Disruptions, July 19-23, 2021). https://tsdw.pppl.gov/Talks/2021/Lehnen.pdf
[6] E.M. Hollmann, I. Bykov, N.W. Eidietis, J.L. Herfindal, A. Lvovskiy, R.A. Moyer, P.B. Parks, C. Paz-Soldan, A.Yu. Pigarov, D.L. Rudakov, D. Shiraki, and J. Watkins, Phys. Plasmas 27, 042515 (2020).
[7] C. Paz-Soldan, N.W. Eidietis, Y.Q. Liu, D. Shiraki, A.H. Boozer, E.M. Hollmann, C.C. Kim, and A. Lvovskiy, Plasma Phys. Control. Fusion 61, 054001 (2019).
[8] E.M. Hollmann, N. Commaux, N. Eidietis, C. Lasnier, D.L. Rudakov, D. Shiraki, C. Cooper, J.R. Martin-Solis, P. Parks, and C. Paz-Soldan, Phys. Plasmas 24, 062505 (2017).
[9] A.N. James, E.M. Hollmann, J.H. Yu, M.E. Austin, N. Commaux, T. Evans, D.A. Humphreys, T.C. Jernigan, P.B. Parks, S. Putvinski, E.J. Strait, G.R. Tynan, and J. Wesley, J. Nucl. Mater. 415, S849 (2011).
[10] D. Shiraki, N. Commaux, L.R. Baylor, C.M. Cooper, N.W. Eidietis, E.M. Hollmann, C. Paz-Soldan, S.K. Combs, and S.J. Meitner, Nucl. Fusion 58, 056006 (2018).
[11] E.M. Hollmann, N.W. Eidietis, J.L. Herfindal, P.B. Parks, A.Y. Pigarov, D. Shiraki, M.E. Austin, L. Bardoczi, L. Baylor, I. Bykov, T.N. Carlstrom, D. Kaplan, C.J. Lasnier, A. Lvovskiy, A. Moser, R.A. Moyer, C. Paz-Soldan, D.L. Rudakov, C. Samuell, M. Shafer, M. Van Zeeland, A. Welander, and R. Wilcox, Nucl. Fusion 59, 106014 (2019).
[12] S. Sridhar, C. Reux, P. Beyer, M. Lehnen, I. Coffey, R. Guirlet, N. Fedorczak, and JET Contributors, Nucl. Fusion 60, 096010 (2020).
[13] J.R. Martin-Solis, A. Loarte, E.M. Hollmann, B. Esposito, V. Riccardo, FTU and DIII-D Teams and JET EFDA Contributors, Nuclear Fusion 54, 083027 (2014).
[14] Y.Q. Liu, P.B. Parks, C. Paz-Soldan, C. Kim, and L.L. Lao, Nucl. Fusion 59, 126021 (2019).
[15] V. Bandaru, M. Hoelzl, C. Reux, O. Ficker, S. Silburn, M. Lehnen, N. Eidietis, JOREK Team, and JET Contributors, Plasma Phys. Control. Fusion 63, 035024 (2021).
[16] M.S. Vorenkamp, A. Nagy, A. Bortolon, R. Lunsford, R. Maingi, D.K. Mansfield, and A.L. Roquemore, Fus. Sci. Tech. 72, 488 (2017).
[17] T. Odstrcil, N.T. Howard, F. Sciortino, C. Chrystal, E. Hollmann, G. McKee, K.E. Thome, and T. Wilks, Phys. Plasmas 27, 082503 (2020).
[18] B. Zurro, E. Hollmann, A. Baciero, M.A. Ochando, F. Medina, K.J. McCarthy, E. Blanco, E. de la Cal, D. Carralero, M.A. Pedrosa, and TJ-II team, Nucl. Fusion 51, 063015 (2011).
[19] E.M. Hollmann, K.R. Umstadter, R.P. Doerner, J. Munoz, D. Nishijima, and A. Yu. Pigarov, J. Nucl. Mater. 415, S425 (2011).
[20] J. L. Luxon, Nucl. Fusion 42, 614 (2002).
[21] M.A. Van Zeeland and T.N. Carlstrom, Rev. Sci. Instrum. 75, 3423 (2004).
[22] J. Chen, W.X. Ding, D.L. Brower, D. Finkenthal, C. Muscatello, D. Taussig, and R. Boivin, Rev. Sci. Instrum. 87, 11E108 (2016).
[23] D.I. Kiramov and B.N. Breizman, Nucl. Fusion 60, 084004 (2020).
[24] E.M. Hollmann, T.C. Jernigan, P.B. Parks, J.A. Boedo, T.E. Evans, M. Groth, D.A. Humphreys, A.N. James, M.J. Lanctot, D. Nishijima, D.L. Rudakov, H.A. Scott, E.J. Strait, M.A. Van Zeeland, J.C. Wesley, W.P. West, W. Wu, and J.H. Yu, Nucl. Fusion 48, 115007 (2008).

[25] J.E. Bailey, G.A. Rochau, R.C. Mancini, A.A. Iglesias, J.J. MacFarlane, E.E. Glovkin, C. Blancard, P. Cosse, and G. Faussurier, Phys. Plasmas 16, 058101 (2009).
[26] M.J. Seaton, "The Theory of Excitation and Ionization by Electron Impact," in Atomic and Molecular Processes, D.R. Bates, Ed. (New York, Academic Press, 1962).
[27] Y.K. Kim, Phys. Rev. A 64, 032713 (2001).
[28] E.M. Hollmann, P.B. Parks, D.A. Humphreys, N.H. Brooks, N. Commaux, N. Eidietis, T.E. Evans, R. Isler, A.N. James, T.C. Jernigan, J. Munoz, E.J. Strait, C. Tsui, J. Wesley, and J.H. Yu, Nucl. Fusion 51, 103026 (2011).
[29] J. Weiland and A. Zagorodny, Rev. Mod. Plasma Phys. 3, 1 (2019).
[30] D.I. Kiramov and B.N. Breizman, Phys. Plasmas 24, 100702 (2017).
[31] J.S. deGrassie, J.A. Boedo, and B.A. Grierson, Phys. Plasmas 22, 080701 (2015).

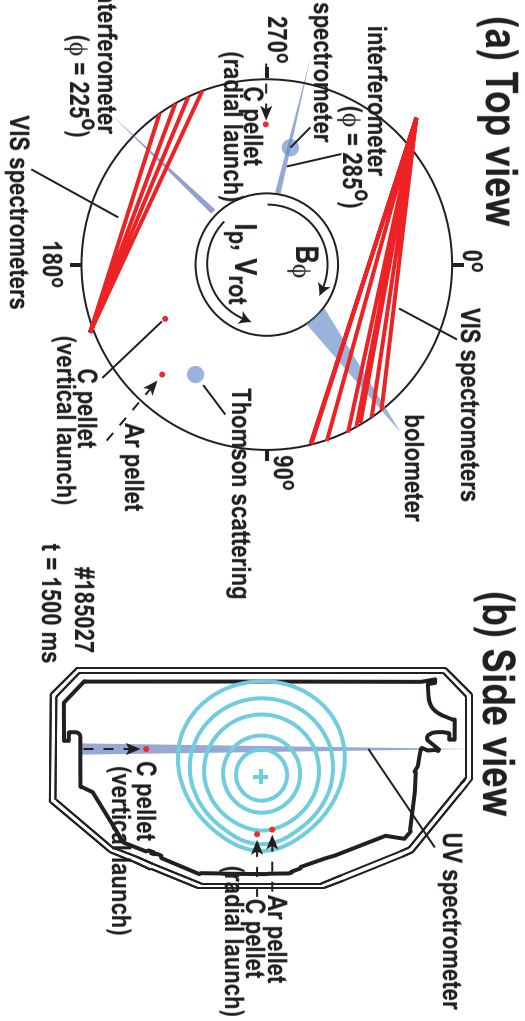

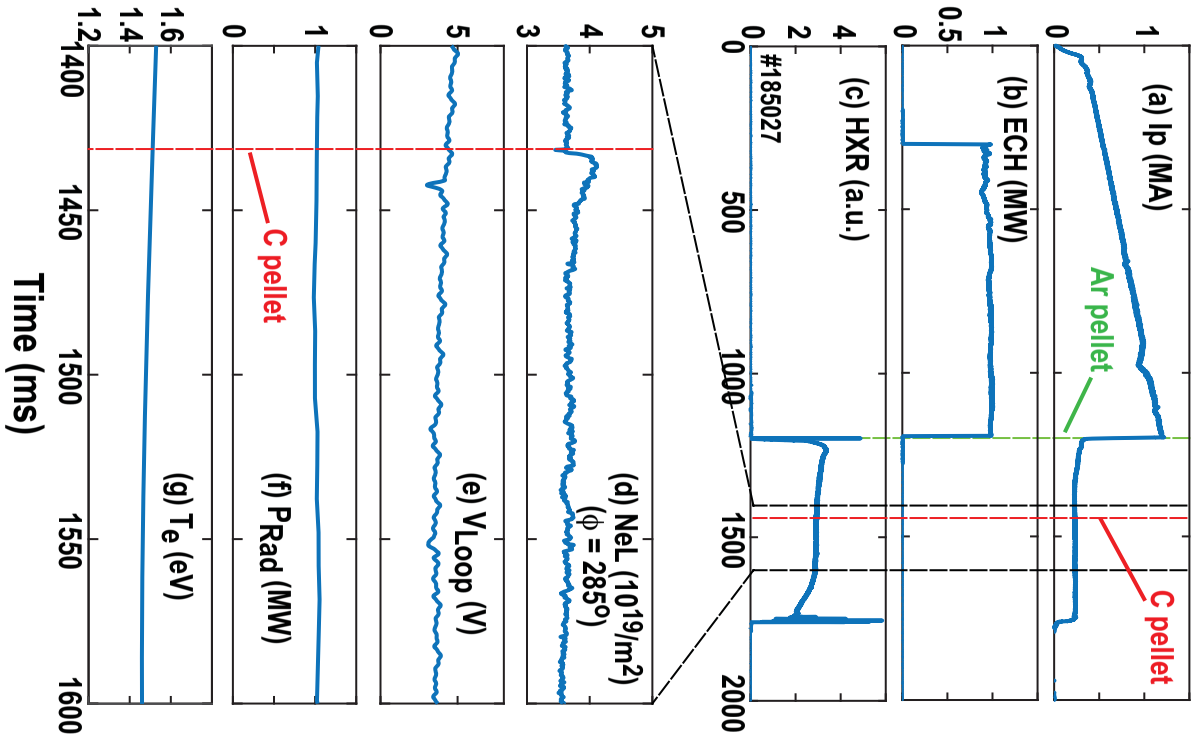

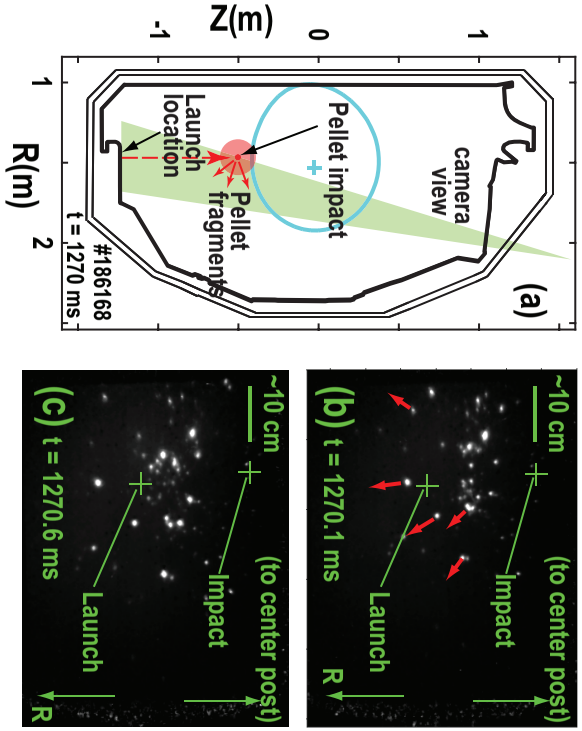

PLEASE CITE THIS ARTICLE AS DOI: 10.1063/5.0080385

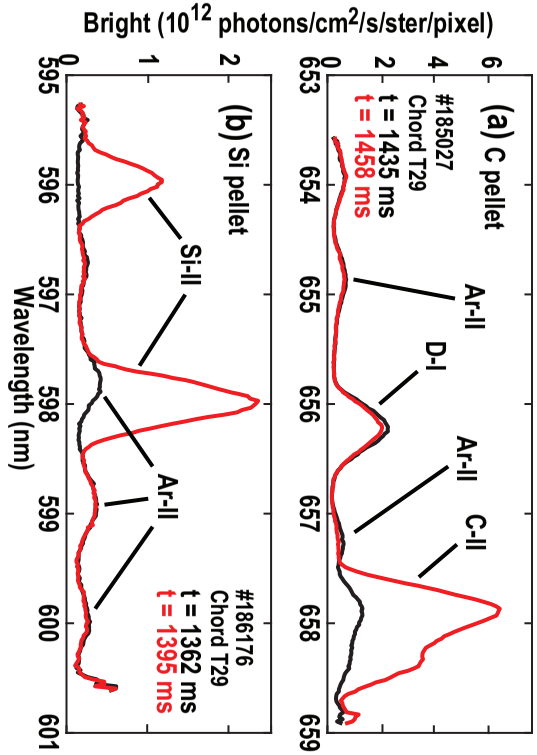

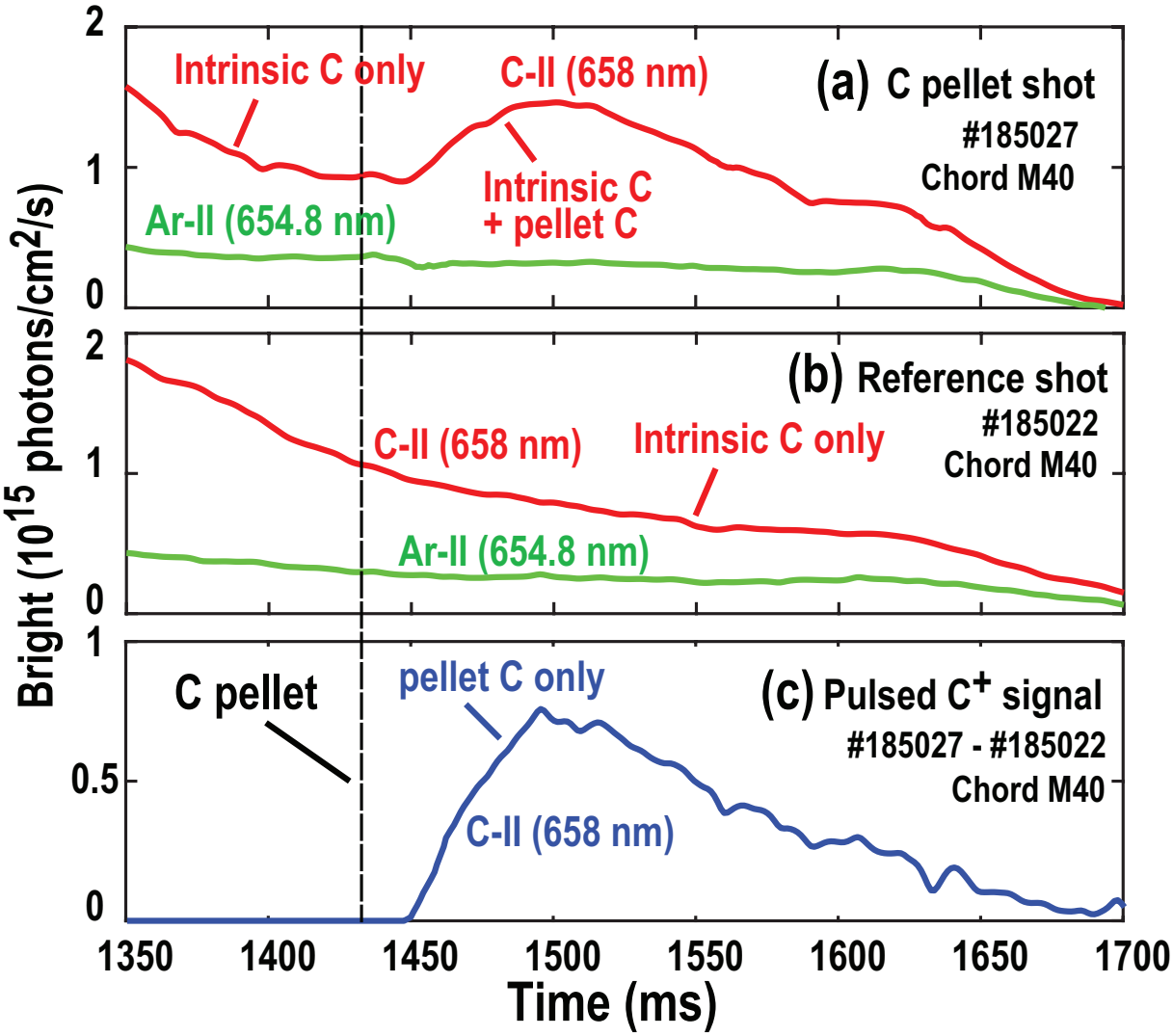

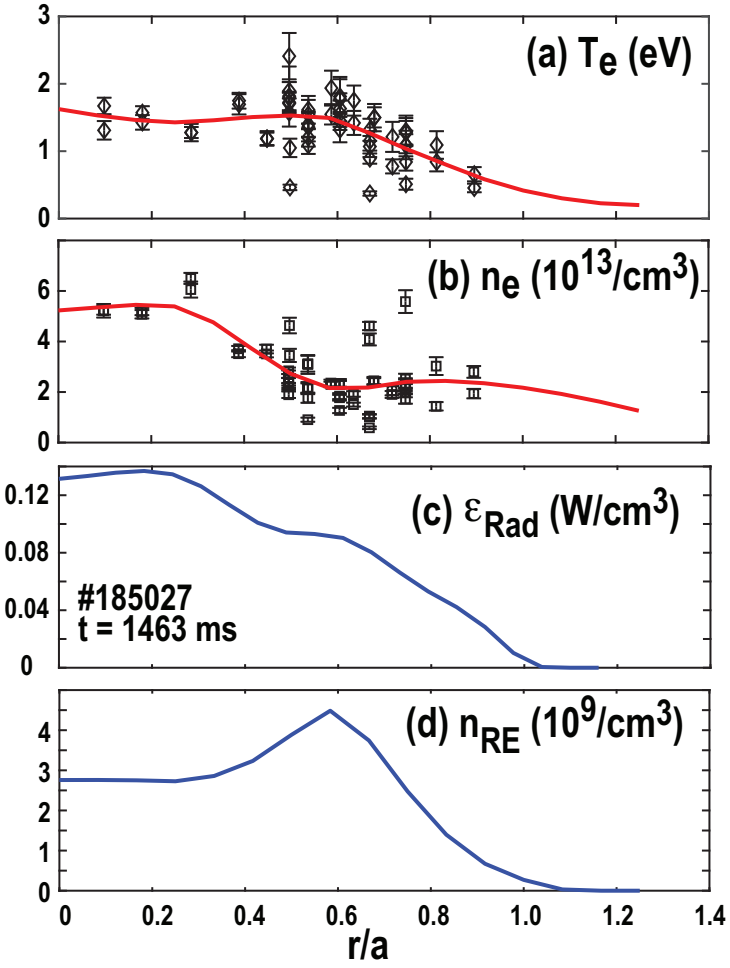

PLEASE CITE THIS ARTICLE AS DOI: 10.1063/5.0080385

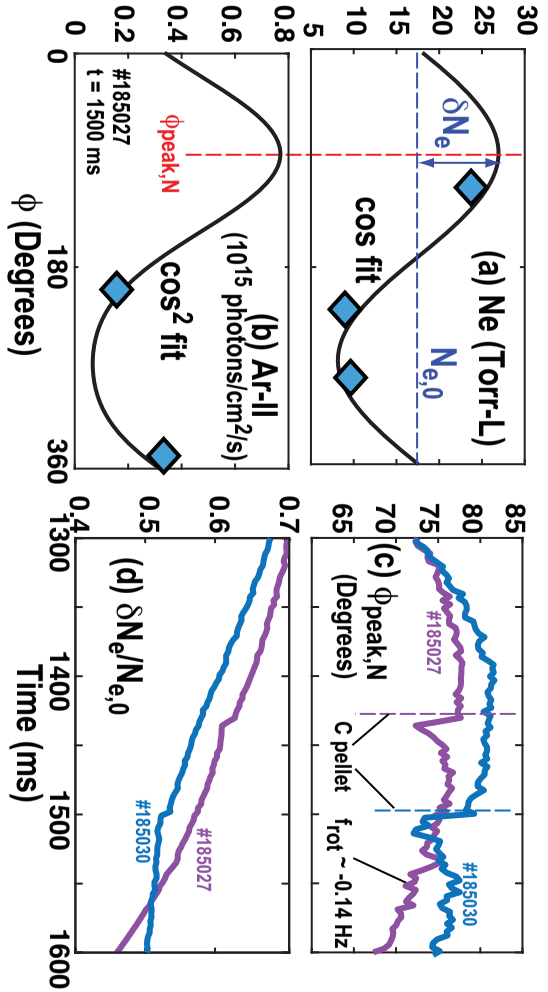

PLEASE CITE THIS ARTICLE AS DOI: 10.1063/5.0080385